Influence of Mn/Fe ratio on electrochemical and structural properties of P2-NaxMn1–yFeyO2 phases as positive electrode material for Na-Ion batteries

Benoit Mortemard de Boisse, Dany Carlier, Marie Guignard, Elodie Guérin, Mathieu Duttine, Alain Wattiaux, Claude Delmas

Influence of the Mn/Fe ratio on the electrochemical and structural properties of P2-$Na_xMn_{1-y}Fe_yO_2$ phases as positive electrode material for Na-ion batteries.

Benoit Mortemard de Boisse, Dany Carlier, Marie Guignard, Elodie Guerin, Mathieu Duttine, Alain Wattiaux and Claude Delmas*.

CNRS, Université de Bordeaux, ICMCB, 33608 Pessac Cedex, France

Abstract

The comparative structural, Mössbauer and electrochemical studies of the $Na_xMn_{2/3}Fe_{1/3}O_2$ and $Na_xMn_{1/2}Fe_{1/2}O_2$ systems show that the change in the Mn/Fe ratio has a significant influence on the overlap between the $Mn^{3+/4+}$ and $Fe^{3+/4+}$ redox couples. The P2-type structure is maintained in the $0.3 < x < 0.8$ domain. For the highest intercalation amount, structural distortions occur due to the Jahn-Teller effect of the Mn^{3+} ions. The macroscopic distortion results from a competition between the opposite effects of Mn^{3+} and Fe^{3+}: the isotropic character of Fe^{3+} tends to prevent the macroscopic distortion. For the lower sodium amounts, the instability of the interstitial trigonal prismatic space leads to the formation, by slab gliding, of a very disordered structure. Even if this structural transition is reversible a strong capacity fading is observed if the cell is charged above 4V vs Na/Na^+.

Introduction

Li-ion batteries are the core of our nomad way of life, powering all our mobile communication devices and electric vehicles. However, Li resources are few and not well distributed; therefore, alternatives need to be found. In this context, Na-ion batteries have drawn a lot of attention for the past 10 years as they represent the best candidate for stationary and large-scale applications where selection criteria are the cost and abundance of raw materials.[1-7]

Among the various materials studied, sodium layered oxides (Na_xMO_2, M = transition metal) represent a promising family[8-10]. The most promising candidates are based on the Mn and / or Fe elements, which are the less expensive ones among the 3d elements: $Na_x(Mn,Fe)O_2$ [11-19], $Na_x(Mn,Ni)O_2$[20-21], $Na_x(Mn,Mg)O_2$[22-24], $Na_x(Mn,Ni, Fe)O_2$[25-27], $Na_x(Mn,Co)O_2$[28-31] $Na_x(Mn,Ni, Co)O_2$ [32-39] ,$Na_x(Li,Ni,Mn)O_2$[39-40].

The bigger size of the Na^+ ion (1.02 Å) compared to that of the Li^+ one (0.76 Å) leads to the formation of various polytypes: P3, P2, O3 depending on the sodium amount and synthesis conditions[41]. Generally, the X-ray powder diffraction (XRPD) patterns of these materials are indexed in the hexagonal system; when a structural distortion occurs (monoclinic or orthorhombic) they are designed by P'3, P'2 or O'3.

In the $Na_xMn_{1-y}Fe_yO_2$ system, only the P2 and O3 polytypes were considered as pristine positive electrode materials. In our previous work we reported the structural changes occurring during the (de)intercalation process from P2-$Na_xMn_{1/2}Fe_{1/2}O_2$[17]. In this study, we extend this approach to the P2-$Na_xMn_{2/3}Fe_{1/3}O_2$ system in order to discuss the impact of the Mn:Fe ratio on the electrochemical properties and on the redox processes from a Mössbauer spectroscopy study. A very good knowledge of their fundamental properties is required in order to optimize them for future applications.

Experimental

The synthesis protocol for the synthesis of P2-$Na_xMn_{1-y}Fe_yO_2$ is described in details in our previous work[12]. Manganese, iron and sodium nitrates were dissolved along with glycine into deionized water. A sodium excess of 10 wt % was used to take into account the high volatility of sodium oxides during the forthcoming heat treatment. The mixture was then heated in a ceramic bowl placed into a sand bath (T ≈ 400°C). The product from the combustion reaction was then ground and heated at 700 °C under air for 20 h and at 1000 °C under O_2 for 5 h. After the heat treatment, the powder was quenched down to RT and introduced into an Ar-filled glovebox to avoid oxidation and reaction with air moisture. The Mn:Fe and Na:M ratios were analyzed by Induced Coupled Plasma – Atomic Emission Spectroscopy.

Synchrotron X-ray powder diffraction (SXRPD) pattern of the starting material was recorded at the Argonne Photon Source (APS, Argonne National Laboratory, IL, USA) at High Resolution powder diffraction beamline (11-BM). The powder was loaded into a 1.5 mm diameter Kapton capillary sealed with epoxy. The wavelength used was equal to 0.41391 Å. Data was recorded three times between 0 and 60° (2θ range) (≈ 50 minutes / pattern) and then merged with a 0.002° step size. The Rietveld refinement of the structure was performed from SXRPD patterns recorded between 0 and 60° though we chose to show only the range corresponding to 10 – 70 ° (2θ Cu kα_1) in the present paper.

The lab XRPD pattern of the discharged material was recorded using a Bruker D5000 diffractometer equipped with a Cu anticathode (Cu k$\alpha_{1,2}$) in the 2θ range of 10 – 120 °. The sample consisted of a 100 mg pellet of active material and carbon black mixture (80/20 weight ratio, diameter 13 mm, pressed for 1 min under 4 tons pressure). The pellet was used as positive electrode in Na/$NaPF_6$ in Propylene Carbonate (PC) /$Na_xMn_{2/3}Fe_{1/3}O_2$ cell that was discharged to 1.5 V and the voltage was maintained until stabilization of the residual current. The cells was then recovered and washed with anhydrous dimethyl Carbonate (Sigma Aldrich, >99% purity) to recover the material.

The electrochemical characterizations were carried out in Na/$NaPF_6$ in Propylene Carbonate (PC)/$Na_xMn_{2/3}Fe_{1/3}O_2$ batteries assembled in 2032 type coin cells. The positive electrode consisted of a mixture of the active material/Carbon Black (CB)/PolyTetraFluoreEthylene (PTFE) in a 77/17/6 weight ratio (total mass ≈ 22 mg). The electrolyte was obtained by dissolution of $NaPF_6$ (Alpha Aesar 99+%) in Propylene Carbonate (PC, Sigma-Aldrich anhydrous 99%) to reach a concentration of 1 mol.l^{-1}. 2 wt % of FluoroEthylene Carbonate (FEC, obtained through an industrial partner) were added to the electrolyte to limit its decomposition at high voltage. All data were recorded using a Biologic VMP3 potentiostat. The electrodes were separated by three layers of Whatman glass fiber sheet to avoid formation of dendrites.

Operando in situ XRPD was carried out using an *in situ* cell purchased from the LRCS, Amiens, France[42] on a Bruker D5000 diffractometer equipped with a Cu target. After a preliminary experiment, the 13 – 20° and 30 – 43° 2θ ranges were selected for the acquisitions during cycling. The cell was previously fully discharged and placed under constant voltage at 1.5 V *vs.* Na^+/Na before recording the full charging process. We therefore started the experiment from a material with the highest intercalated Na amount. The current rate was C/100 and the XRPD pattern were recorded every Δx_{Na} = 0.01. The electrochemical data were controlled and recorded using a Biologic VMP3 potentiostat. All the voltages mentioned in the present paper are expressed *versus* the Na^+/Na redox couple.

^{57}Fe Mössbauer measurements were performed using a constant acceleration Halder-type spectrometer operating in transmission geometry with a room temperature ^{57}Co source (embedded in Rh matrix). The velocity scale was calibrated according to the ^{57}Fe Mössbauer spectrum of a pure α-Fe^0 foil recorded at room temperature. The samples were prepared using the same protocol as described before for the XRPD pattern of intercalated $Na_xMn_{2/3}Fe_{1/3}O_2$.

After grinding, the samples were introduced in airtight sample holders. The refinement of Mössbauer hyperfine parameters (δ isomer shift, Δ quadrupole splitting, Γ signal linewidth and relative areas) was performed using both homemade programs and the WinNormos® software (Wissenschaftliche Elektronik GmbH). In this study, all Mössbauer signals were analysed using a distribution of the quadrupole splitting (Δ) parameter following the method proposed by Hesse and Rübartsch[43]. Thus, each sub-spectrum is considered as a sum of discrete quadrupole doublets with same isomer shift, same Lorentzian line width (Γ = 0.25 mm/s) but different values of the quadrupole splitting parameter.

Results

Structure of the pristine material

In this study, the targeted composition was $Na_{2/3}Mn_{2/3}Fe_{1/3}O_2$. This material was characterized by XRD diffraction. The auto-combustion type synthesis route leads to a pure phase with a very good crystallinity, as previously reported[12]. Its structure was determined from synchrotron data. The XRD pattern is shown in **Figure 1**, along with the calculated one resulting from the structural Rietveld refinement. The cell parameters in the $P6_3/mmc$ space group (a_{hex} = 2.9400(1) Å and c_{hex} = 11.1812(6) Å) are close to those of the literature on similar compositions[15]. Refinement of the structure gives the sodium content in the material: 0.66(4). This composition is confirmed by ICP-AES analysis. In the following, we will therefore refer to our material as P2-$Na_{0.66}Mn_{2/3}Fe_{1/3}O_2$. The Rietveld parameters are given in Table S1 and compared to those previously obtained from the P2-$Na_{0.62}Mn_{1/2}Fe_{1/2}O_2$ composition. For both materials the Na ADP values are quite large; this is certainly due to the high mobility of Na^+ ions, in the P2 type structure, which can exchange between the two prismatic face-sharing sites.

Detailed comparison of the structural parameters (unit cells, oxygen atomic positions and occupancy of the two types of sodium sites) of the $Na_{0.66}Mn_{2/3}Fe_{1/3}O_2$ and $Na_{0.62}Mn_{1/2}Fe_{1/2}O_2$ phases shows that they are almost identical. In fact the change in atomic distances resulting from the change in Mn:Fe ratio is compensated by the change in Mn^{4+}:Mn^{3+} ratio ($Na_{0.62}Mn^{3+}_{012}Mn^{4+}_{0.38}Fe^{3+}_{0.5}O_2$ vs $Na_{0.66}Mn^{3+}_{0.33}Mn^{4+}_{0.34}Fe^{3+}_{0.33}O_2$). Moreover, the sodium distribution is directly related to the amount of vacancies which allows Na to occupy the 2 types of sites without prism face sharing.

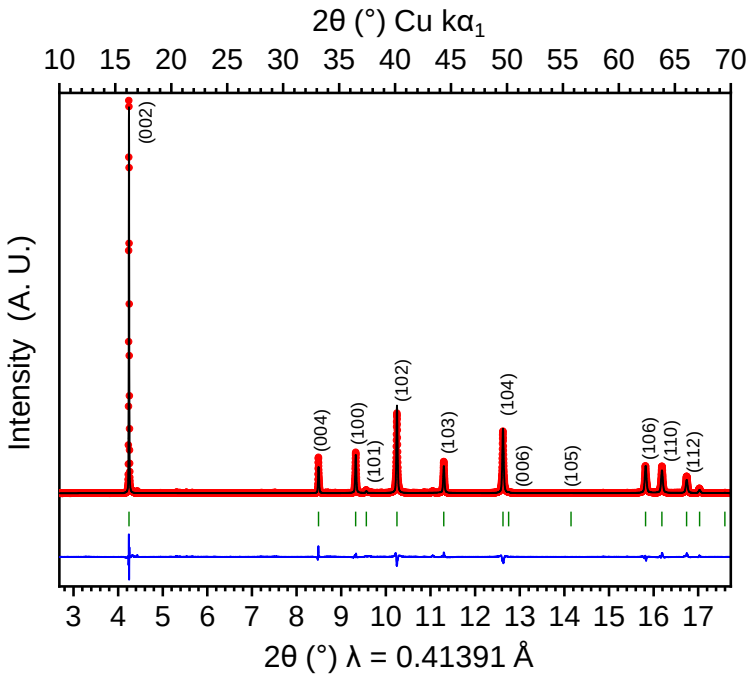

Figure 1: Observed and calculated (Rietveld method) synchrotron XRPD patterns for the P2-$Na_{0.66}Mn_{2/3}Fe_{1/3}O_2$ pristine material. Red dots: experimental, black line: calculated, blue line: difference and green bars: Bragg positions.

Electrochemical behaviour

The electrochemical properties of P2-$Na_{0.66}Mn_{2/3}Fe_{1/3}O_2$ as positive electrode material for Na-ion batteries were investigated in various voltage ranges. The galvanostatic curves recorded at C/20 between 1.5 – 4.0 V and 1.5 – 4.3 V are given in **Figure 2a-b**, in comparison to those obtained from the P2-$Na_{0.62}Mn_{1/2}Fe_{1/2}O_2$ phase (**Fig. 2c-d)**[17]. The shapes of the voltage curves are globally similar. During the first discharge, a reversible voltage plateau is observed at ≈ 2.1 V, consistent with a P2 → P'2 structural transition. The same plateau is observed at ≈ 2.2 V in the following charge. If the cut-off voltage is set to 4.0 V, the following discharge shows the reversibility of the Na^+ (de)intercalation process with a small polarization. When the cut-off voltage is increased to 4.3 V, a second voltage plateau is observed at ≈ 4.15 V. This plateau is not visible on the next discharge and instead an increase of the polarization is observed. Then, the (de)intercalation process is reversible in the whole cycling range but with a large polarization in discharge above 3.2 V. For every experiment, the 2nd, 3rd and 4th cycles are very similar. The comparison of the shape of the charge curves shows that the strong voltage increase, which was observed around x = 0.5 in the P2-$Na_xMn_{1/2}Fe_{1/2}O_2$ phase, occurs around x = 0.3 in the $Na_xMn_{2/3}Fe_{1/3}O_2$ system.

This behaviour suggests, as expected, that the $Mn^{3+/4+}$ couple is involved at low voltage while the $Fe^{3+/4+}$ couple is observed at high voltage. Nevertheless, in the case of the $Na_xMn_{2/3}Fe_{1/3}O_2$ system the break in the curve is less pronounced.

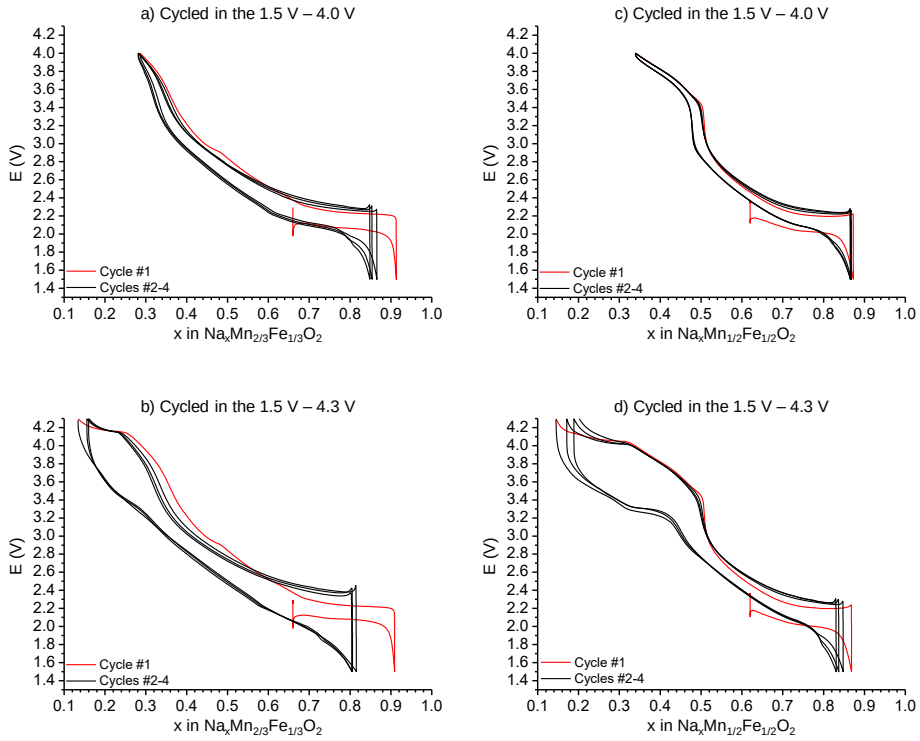

Figure 2: Galvanostatic cycling curves associated to the $Na_xMn_{2/3}Fe_{1/3}O_2$ and $Na_{0.62}Mn_{1/2}Fe_{1/2}O_2$ systems and recorded (a,c) between 1.5 and 4.0 V; (b,d) between 1.5 and 4.3 V at C/20.

To better evaluate the shape of the voltage curves we carried out GITT measurements, **(Fig. 3)**. For both materials, a reversible voltage plateau indicating the occurrence of a two phase domain is observed in discharge around 2.1 V. Upon charge in the $Na_xMn_{2/3}Fe_{1/3}O_2$ system **(Fig. 3a)** for x < 0.76, we observe a continuous increase of the voltage up to x = 0.28. Then a second plateau is observed at E = 4.15 V, followed by a smooth increase of the voltage up to E = 4.3 V. In many Na_xMO_2 layered oxide, this plateau is responsible for the huge increase of the polarization in the following discharge. Looking closely in the 0.28 < x < 0.76 range, one can see two discontinuities in the voltage profile. Two small voltage bumps corresponding to x = 2/3 and ½ are evidenced **(red arrows in Fig. 3a)**. The origin of these accidents is still unknown but could correspond to Na/□ ordering tendencies in the interslab; given the compositions were they occur[44]. The last bump is observed for x ≈1/3 and consists in an increase of the polarization, from 33 mV (x = 0.38) to 49 mV (x = 0.33). The polarization then decreases to 23 mV (x = 0.31) **(insert in Fig. 3a)**.

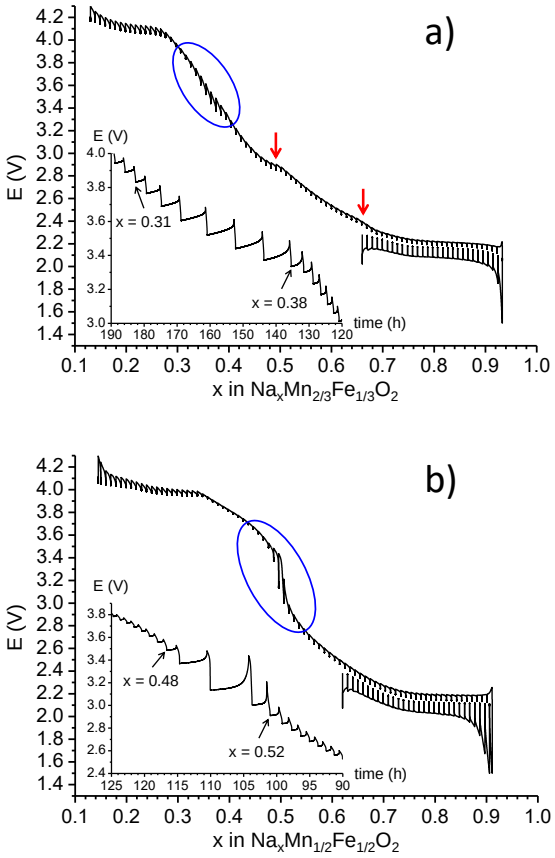

Figure 3: GITT cycling curves recorded with steps of ≈ 0.01 Na^+ per formula unit and a $\Delta V < 4$ mV.h^{-1} relaxation condition for the $Na_xMn_{2/3}Fe_{1/3}O_2$ (a) system. The red arrows indicate slight variation in the slope of the curve. The GITT cycling curve recorded for the $Na_xMn_{1/2}Fe_{1/2}O_2$ system is given in (b) for comparison.

This phenomenon was already observed in the $Na_xMn_{1/2}Fe_{1/2}O_2$ system (Fig. 3b)[17]. Its origin lies in the change of the active redox process, from $Mn^{3+} \rightarrow Mn^{4+}$ to $Fe^{3+} \rightarrow Fe^{4+}$ and is linked to the difficult electronic transfer between Mn^{4+} and Fe^{3+} ions when all Mn^{n+} ions are in the +IV state and all the Fe^{n+} ions are in the +III one. It is however surprising that no voltage jump is observed for the $Na_xMn_{2/3}Fe_{1/3}O_2$ system contrarily to the $Na_xMn_{1/2}Fe_{1/2}O_2$ one. This observation suggests overlap between the redox potential of the Fe^{4+}/Fe^{3+} and Mn^{4+}/Mn^{3+} redox couples for P2-$Na_{0.66}Mn_{2/3}Fe_{1/3}O_2$ while in the case of the $Na_{0.50}Mn_{1/2}Fe_{1/2}O_2$ phase the two redox couples have different values. This point will be further discussed.

The impact of the cut-off voltage on the long-term cycling is shown in **Figure 4a**. Logically, the discharge capacity increases with the cut-off voltage: from 140 mAh.g^{-1} (1.5 – 3.8 V) to 150 mAh.g^{-1}(1.5 – 4.0 V) and to 180 mAh.g^{-1} (1.5 – 4.3 V). After 50 cycles however, a different trend is observed. While the experiments carried out in the 1.5 – 3.8 V and 1.5 – 4.0 V ranges show good capacity retentions of 86 % and 82 %, respectively, increasing the cut-off voltage to 4.3 V leads

to poor capacity retention of 66 % and to similar discharge capacity to that of the experiment carried out in the 1.5 – 3.8 V range (≈ 120 mAh.g^{-1} after 50 cycles). Such a feature is common to many sodium layered oxide materials and is usually induced by structural transitions occurring at high voltage. This part will be further discussed. The similar trend was observed for the $Na_xMn_{1/2}Fe_{1/2}O_2$ phase (**Fig. 4b)**. Nevertheless, the capacity after 50 cycles is, whatever the voltage range, higher for the $Na_xMn_{2/3}Fe_{1/3}O_2$ phase. This difference in behaviour is illustrated in **Figure 5c** which gives a comparison of the charge curves of the two materials **(Fig. 4c)**. It shows that the oxidation before the high voltage plateau is easier in the material with the highest amount of Mn^{3+} ($Na_xMn_{2/3}Fe_{1/3}O_2$).

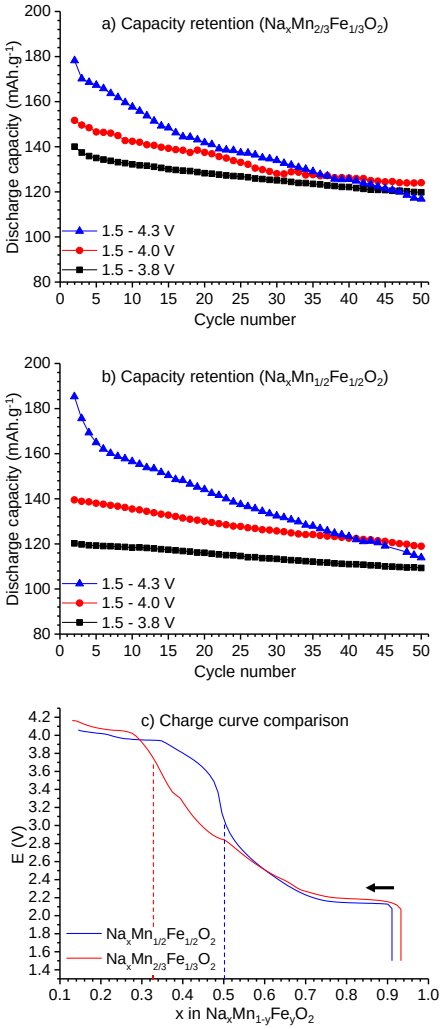

Figure 4: Evolution of the discharged capacities for the P2-based $Na_xMn_{2/3}Fe_{1/3}O_2$ (a) and (b) $Na_xMn_{1/2}Fe_{1/2}O_2$systems in the 1.5 – 3.8 V, 1.5 – 4.0 V and 1.5 – 4.3 V ranges.
(c) Galvanostatic charge curves of batteries recorded at C/20: (blue) $Na_xMn_{1/2}Fe_{1/2}O_2$ and (red) $Na_xMn_{2/3}Fe_{1/3}O_2$. The dashed lines represent the expected position of the voltage jump associated to the change of redox process during charge if the redox potentials of Fe^{4+}/Fe^{3+} and Mn^{4+}/Mn^{3+} are well separated.

In situ XRPD during the charge of the battery

To get a better knowledge of the structural mechanisms involved upon cycling for $Na_xMn_{2/3}Fe_{1/3}O_2$ we conducted an *operando in situ* XRPD experiment. The evolution of the XRPD patterns along with the complete charge of the battery is shown in **Figure 5 and S1** (in reverse order). The evolution of the interslab distance and of the a_{hex}, a_{orth} and b_{orth} cell parameters deduced from the XRPD patterns is given in **Figure S2**.

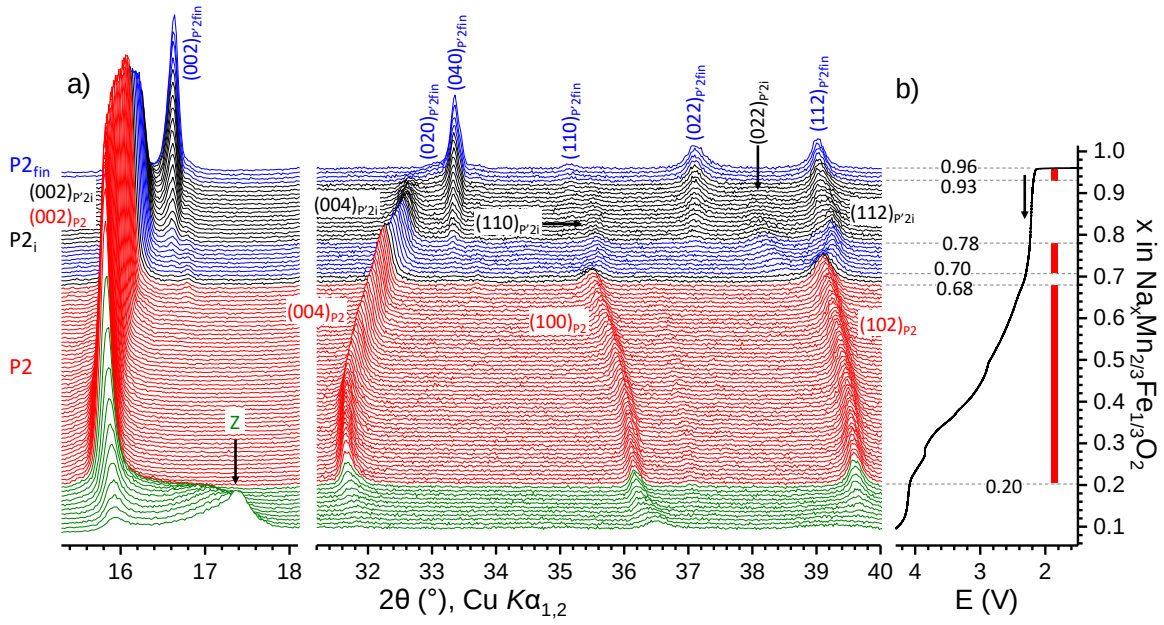

Figure 5: XRPD patterns of the $Na_xMn_{2/3}Fe_{1/3}O_2$ material recorded *in situ* (*operando* mode) during the charge of a $Na_xMn_{2/3}Fe_{1/3}O_2/NaPF_6$ in PC (1M) + 2 wt% FEC/Na cell along with (b) the corresponding cycling curve. The various structural domains are indicated by different colors. The P2-solid solution domains is indicated by the red lines.

The experiment starts from the fully intercalated state of the material: $Na_{0.96}Mn_{2/3}Fe_{1/3}O_2$. Its structure can be indexed in the orthorhombic system of the P'2 structure (Cmcm space group). The orthorhombic distortion is clearly emphasized by the splitting of the $(102)_{P2}$ diffraction line into the $(022)_{P'2}$ and $(112)_{P'2}$ ones. This structure will be further described in detail. The P'2-$Na_xMn_{2/3}Fe_{1/3}O_2$ structure is observed alone for a narrow Na range: $0.93 < x \leq 0.96$. For $x \leq 0.93$, a new set of diffraction lines appears at 16.3° ,32.6° and 38.1°. These diffraction peaks correspond to the $(002)_{P'2}$ and $(022)_{P'2}$ reflections of a newly formed P'2 phase. To differentiate the two P'2 phases, they will be referred to as the "fully-intercalated $P'2_{fin}$ phase" and as the "intermediate

P'2_i phase". The biphasic domain between the two P'2 phases is observed for 0.78 < x < 0.93. Then, the intermediate P'2i phase is observed alone in a short range: 0.70 ≤ x ≤ 0.78. The formation of this intermediate phase is confirmed by a GITT in situ X-Ray experiment realized in the 0.65 < x < 1 composition range **(Fig.S3)**.

Upon further deintercalation, the P2 phase appears through a P2 + P'2_i biphasic domain in the 0.68 < x ≤ 0.70 range. The P2 phase and the intermediate P'2_i have very close interslab distances as shown by the position of their (00*l*) diffraction lines in **Figures 5 and S2**. This results from the small difference in the sodium content. The observation of two P'2 phases in the 0.70 < x ≤ 0.96 domain is clearly new. The comparison of their cell parameters (**Fig. S2**) indicates that P'2_{fin} is more distorted, as the M-M distances in the MO_2 slabs are approximatively equal to 2.91 Å and 3.10 Å *vs.* 2.90 Å and 2.99 Å in the P'2_i phase. These distances are directly determined from the orthorhombic cell parameters. This behaviour is due to the higher Mn^{3+} content in the intercalated P'2_{fin} phase which leads to an increase of the cooperative Jahn-Teller effect. The lower interslab distance of the intercalated P2_{fin} phase (5.40 Å *vs.* 5.45 Å for the intermediate P'2_i phase) confirms this assumption as it implies a higher Na^+ – and thus Mn^{3+}– content.

The magnifications of the *in situ* XRPD patterns in the 0.6 ≤ x ≤ 1 range are given in **Figure 6** for both $Na_xMn_{2/3}Fe_{1/3}O_2$ and $Na_xMn_{1/2}Fe_{1/2}O_2$ systems. They highlight the difference in the P'2 ↔ P2 transition mechanisms between the two systems: while $Na_xMn_{1/2}Fe_{1/2}O_2$ shows a biphasic domain for 0.85 < x ≤ 0.95, followed by a P2 solid solution (x ≤ 0.80) **(Fig. S4)**; the P'2 ↔ P2 phase transition in $Na_xMn_{2/3}Fe_{1/3}O_2$ occurs in the two successive steps. As shown in Fig. 6b, upon charge, the position of the $(002)_{P'2i}$ diffraction line changes continuously. This shows that the intermediate phase contains an increasing number of undistorted MO_2 slabs within the P'2_i phase during the battery charge. This is an evidence of the formation of stacking faults due to the formation of one phase into the other one.

In the P2 solid solution domain, the interslab distance continuously increases as Na^+ ions are involved in the screening effect between the O planes **(Fig. S4)**. On the other hand, the value of the a_{hex} cell parameter continuously decreases due to the contraction of the MO_6 octahedra upon the $M^{3+} \rightarrow M^{4+}$ redox process, the M^{4+}-O bonds being more covalent than the M^{3+}-O one and radius decreases.

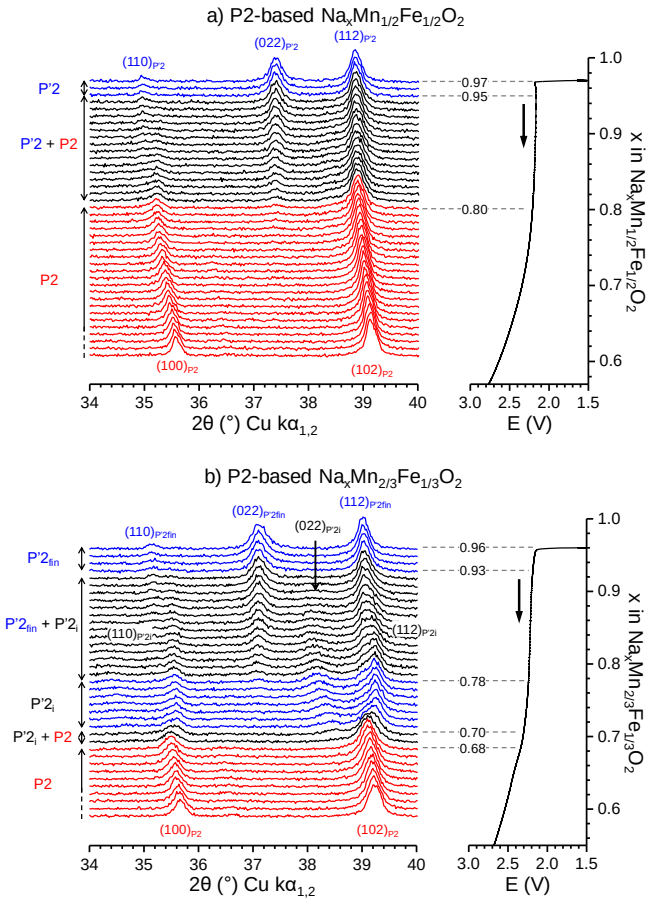

Figure 6: Enlargement of the XRPD patterns of the $Na_xMn_{2/3}Fe_{1/3}O_2$ and $Na_xMn_{1/2}Fe_{1/2}O_2$ material recorded *in situ* (*operando* mode) in the highly intercalated domain showing the formation of $P'2_{fin}$ and and $P'2_i$ phases.

For x < 0.20, there is a continuous decrease of the intensity of the diffraction lines of the P2 phase **(Fig. 5)**. Simultaneously, a broadening of the $(002)_{P2}$ diffraction peak is observed on the high angle side and a new diffraction peak appears in the 16.7 ≤ 2θ ≤ 16.9 ° region. This peak is attributed to a phase we will refer as "Z" as in our previous study of the $Na_xMn_{1/2}Fe_{1/2}O_2$ system[17].The P2 → "Z" transition mechanism at the end of charge is occurs through the creation of stacking faults, consisting in layers of $Na_\varepsilon O_6$ or $\square O_6$ octahedra, created among the P2 layers in the material. The asymmetry of the (002) line on the small 2θ values shows that some prismatic layers are remaining in this material contrarily to what it is observed in the $Na_xMn_{1/2}Fe_{1/2}O_2$ system[17].

Structure of the intercalated material

The structure of P'2-$Na_{0.96}Mn_{2/3}Fe_{1/3}O_2$ was investigated by *ex situ* XRPD. The XRPD pattern is successfully indexed in the Cmcm space group. The experimental and calculated (Rietveld method) patterns are shown in **Figure S5** with the corresponding cell and atomic parameters.

The b_{orth}/a_{orth} ratio (1.88) suggests the orthorhombic distortion *vs.* the ideal un-distorted phase ($b_{orth}/a_{orth} = \sqrt{3}$). This distortion is confirmed by the M-O distances in the MO_6 octahedra. These values are reported in Table 1 in comparison with those obtained for P2-$Na_1Mn_{1/2}Fe_{1/2}O_2$[17] and O'3-$NaMnO_2$[45]. The $a_{orth.}/b_{orth.}$ and $a_{mon.}/b_{mon.}$ ratios which are good indicators of the structural distortion are also reported. As the Mn^{3+} accounts for only 63% of the total transition metal ions in the material, the distortion is lower than that observed for the O'3 $NaMnO_2$ phase. The presence of 1/3 Fe^{3+} in the material, which is strongly stabilized in an ideal octahedral environment, prevents from a too large distortion. In the case of the P'2-$Na_{\approx 1}Mn_{1/2}Fe_{1/2}O_2$ the mean octahedron distortion is smaller, as expected, due to the lower amount of Mn^{3+} and to the higher amount of iron.

In the P'2-$Na_{0.96}Mn_{2/3}Fe_{1/3}O_2$, only one type of prismatic NaO_6 site: Na_e(sharing edges with the surrounding MO_6 octahedra) is occupied while the face sharing Na_f site remains vacant, as a result of the simultaneous minimization of the Na^+-Na^+ and Na^+-M^{n+} repulsions.

	Mn-O short bonds	Mn-O long bonds	b/a(orth.) or a/b (mon.)
P'2 – $Na_1(Mn_{1/2}Fe_{1/2})O_2$[17] Cmcm	4 x 1.99 Å	2 x 2.18 Å	1.84
P'2 – $Na_{0.96}(Mn_{2/3}Fe_{1/3})O_2$ Cmcm	4 x 2.01Å	2 x 2.25 Å	1.88
O'3 $NaMnO_2$[45] C2/m	4 x 1.94 Å	2 x 2.39 Å	1.97

Table 1. Comparison of the Mn-O bond lengths in Jahn-Teller distorted manganese layered oxides. The departure of the a/b(mon.) and b/a(orth.) from $\sqrt{3}$ characterizes the in plane distortion due to the Jahn-Teller effect.

Redox mechanisms study

We investigated the redox mechanisms in both the $Na_xMn_{2/3}Fe_{1/3}O_2$ and $Na_xMn_{1/2}Fe_{1/2}O_2$ systems by ^{57}Fe Mössbauer spectroscopy. In this paper we only focus on the comparative redox behavior, a detailed characterization of the analyzed phases will be published elsewhere. By nature, the Mössbauer spectroscopy is directly sensitive to the iron oxidation state and indirectly to the change in the Mn^{4+}/Mn^{3+}, ratio through the quadrupolar splitting that is affected by the Jahn-Teller distortion of Mn^{3+} ions.

As expected, in both starting materials (P2-$Na_{0.66}Mn_{2/3}Fe_{1/3}O_2$ and P2-$Na_{0.62}Mn_{1/2}Fe_{1/2}O_2$) iron is in the trivalent state. Indeed, the Mössbauer spectra of the pristine materials **(Fig. 7a and 7b)** can be described by one quadrupole doublet characterized by an isomer shift (δ) of 0.35 mm/s consistent with high-spin Fe^{3+} ions in FeO_6 octahedral environment. Furthermore, both spectra were reconstructed using a distribution of the quadrupole splitting parameter (Δ), which led to an excellent fit to the experimental data. Such distributions arise from some cationic disorder (heterogeneous repartition of Na^+, Fe^{3+} and $Mn^{3+/4+}$ around the local probe) and local distortions of the FeO_6 octahedra due to the presence of Mn^{3+} Jahn-Teller ions in the iron vicinity (second coordination sphere or first cationic neighbors). The higher (average) value of the quadrupole splitting (Δ^* = 0.81 mm/s, see **Table 2**) is actually observed for the "$Mn_{2/3}Fe_{1/3}$" phase presenting the higher Mn^{3+} content (33%).

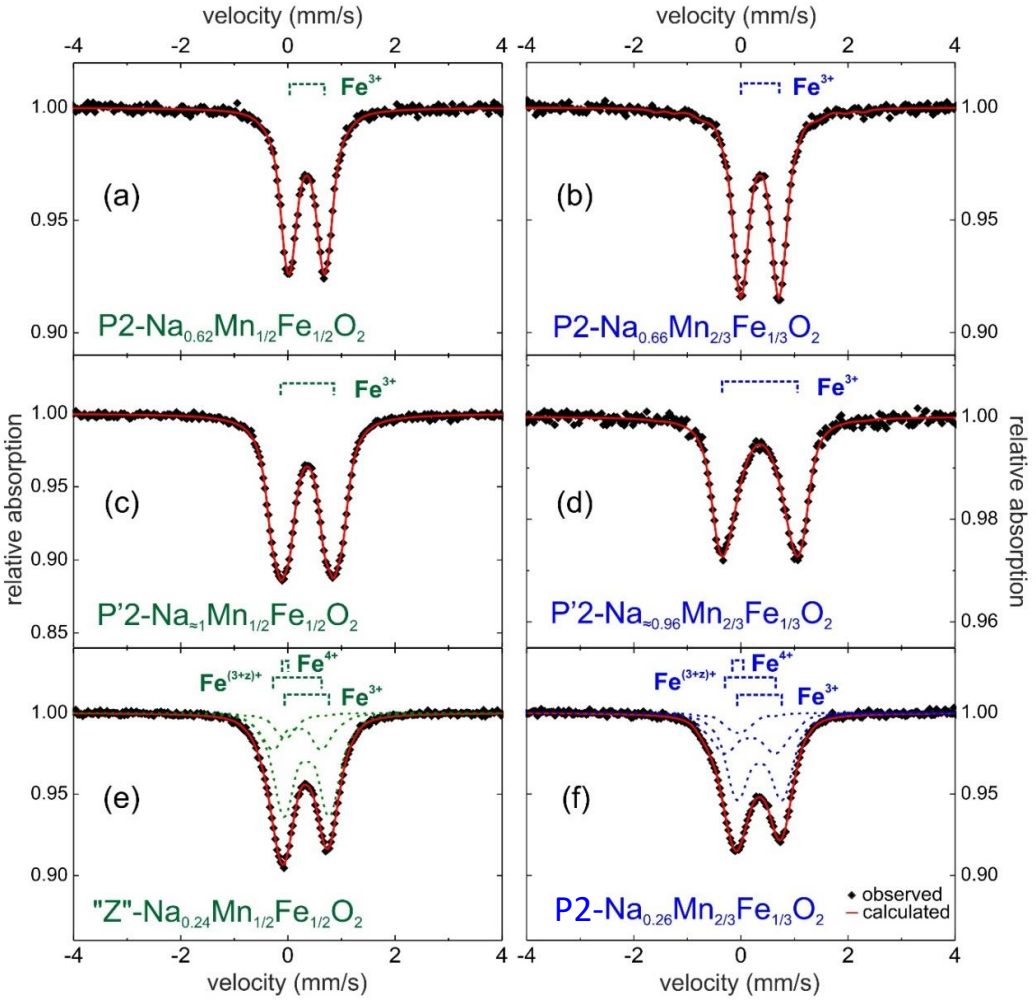

Figure 7: Room temperature ^{57}Fe Mössbauer spectra of (a) P2-$Na_{0.62}Mn_{1/2}Fe_{1/2}O_2$, (b) P2-$Na_{0.66}Mn_{2/3}Fe_{1/3}O_2$, (c) P'2-$Na_{\approx1}Mn_{1/2}Fe_{1/2}O_2$, (d) P'2-$Na_{\approx0.96}Mn_{2/3}Fe_{1/3}O_2$, (e) "Z"-$Na_{0.24}Mn_{1/2}Fe_{1/2}O_2$ and (f) "Z"-$Na_{0.26}Mn_{2/3}Fe_{1/3}O_2$. Dashed lines indicate that the associated Mössbauer signals were calculated considering a quadrupole splitting distribution.

The observed and calculated spectra of some intercalated and deintercalated materials are compared to the pristine ones in **Figure 7** and the associated Mössbauer parameters are gathered in **Table 2**. All spectra show an apparent quadrupole doublet whose asymmetry, shift and splitting vary with the state of charge.

The Mössbauer spectra of the intercalated materials (P'2-$Na_{1.0}Mn_{1/2}Fe_{1/2}O_2$ and P'2-$Na_{0.96}Mn_{2/3}Fe_{1/3}O_2$) (**Fig. 7c and 7d**) were also successfully reconstructed with a distribution of quadrupole doublets, whose isomer shift (δ = 0.36 mm/s) is characteristic of six-fold Fe^{3+} ions. As for the pristine materials, the wider distribution and the higher average value of the quadrupole splitting parameter (Δ^* = 1.31 mm/s, **Table 2**) are observed for the phase presenting the higher Mn^{3+} content (62% for the "$Mn_{2/3}Fe_{1/3}$" phase as compared to 50% for the "$Mn_{1/2}Fe_{1/2}$" one). The highest amount of Mn^{3+} ions is, the largest cooperative (for these intercalated phases) Jahn-Teller distortion of the Fe^{3+} octahedra is and then, the largest quadrupole effect is. Moreover, the intercalation of Na^+ ions may also be responsible of an additional disorder in the local environment of iron inducing slight variations of the Electric Field Gradient (EFG) at the iron nuclei and thus, a broadening of the quadrupole splitting distribution.

Expected results from electrochemistry			Mössbauer results					
$Na_xMn_{2/3}Fe_{1/3}O_2$ system								
Developed formula	% Fe^{3+}	% Fe^{4+}		δ (mm/s)	Δ* (mm/s)	A (%)	% Fe^{3+}	% Fe^{4+}
P'2-$Na_{0.96}Mn^{3+}_{0.62}Mn^{4+}_{0.04}Fe^{3+}_{0.33}Fe^{4+}_{0.00}O_2$	100	0	Fe^{3+}	0.358(2)	1.31	100	100	0
P2-$Na_{0.66}Mn^{3+}_{0.33}Mn^{4+}_{0.34}Fe^{3+}_{0.33}Fe^{4+}_{0.00}O_2$	100	0	Fe^{3+}	0.354(2)	0.81	100	100	0
P2-$Na_{0.26}Mn^{3+}_{0.00}Mn^{4+}_{0.67}Fe^{3+}_{0.26}Fe^{4+}_{0.07}O_2$	79	21	Fe^{3+}	0.35(3)	0.79	59(3)	77	23
			$Fe^{(3+z)+}$	0.17(5)	0.94	33(3)		
			Fe^{4+}	-0.05(2)	0.38	8(3)		
$Na_xMn_{1/2}Fe_{1/2}O_2$ system								
Developed formula	% Fe^{3+}	% Fe^{4+}		δ (mm/s)	Δ* (mm/s)	A (%)	% Fe^{3+}	% Fe^{4+}
P'2-$Na_{1.00}Mn^{3+}_{0.50}Mn^{4+}_{0.00}Fe^{3+}_{0.50}Fe^{4+}_{0.00}O_2$	100	0	Fe^{3+}	0.362(2)	0.98	100	100	0
P2-$Na_{0.62}Mn^{3+}_{0.12}Mn^{4+}_{0.38}Fe^{3+}_{0.50}Fe^{4+}_{0.00}O_2$	100	0	Fe^{3+}	0.350(2)	0.68	100	100	0
"Z"-$Na_{0.24}Mn^{3+}_{0.00}Mn^{4+}_{0.50}Fe^{3+}_{0.34}Fe^{4+}_{0.26}O_2$	68	32	Fe^{3+}	0.35(1)	0.85	67(3)	80	20
			$Fe^{(3+z)+}$	0.17(3)	0.92	24(3)		
			Fe^{4+}	-0.05(3)	0.32	9(3)		

Table 2: ^{57}Fe Mössbauer hyperfine parameters corresponding to the fit of the spectra presented in figure 7. δ: isomer shift relative to α-Fe at room temperature, Δ^*: mean value of the quadrupole splitting distribution (Lorentzian line width : 0.25 mm/s) and A: relative area. For the $Fe^{(3+z)+}$ sub-spectra, the relative proportion of Fe^{3+} and Fe^{4+} was roughly estimated taking into account the calculated isomer shift values of the three subspectra. *Average value of the quadrupole splitting distribution.

For both deintercalated phases ($x \approx 0.25$), additional sub-spectra (compared to the pristine materials) are required to account for the apparent asymmetry and the shift towards lower velocities of the Mössbauer spectra (**Fig. 7e and 7f**). The refinement of hyperfine parameters clearly indicates a partial oxidation of iron. Indeed, the best fit to experimental data was obtained considering three quadrupole doublets associated with iron at various oxidation states: Fe^{3+} (δ = 0.35 mm/s), Fe^{4+} (δ = -0.05 mm/s) and $Fe^{(3+z)+}$ (δ = 0.17 mm/s) (**Table 2**). For the "Z"-$Na_{0.24}Mn_{1/2}Fe_{1/2}O_2$ phase the amount of tetravalent iron ions is sligtly smaller than the expected value deduced from the eletrochemical deintercalation. As this material was recovered at 4.3 V vs Na/Na^+ the detemined x value can be smaller than the real one due to an electrolyte decomposition. The presence of this last intermediate oxidation state was previously reported in the $Li_xNi_{0.70}Fe_{0.15}Co_{0.15}O_2$ systems[47].

Discussion

The aim of the following discussion is to evaluate the impact of the Mn/Fe ratio on the electrochemical and structural properties from the comparison between the $Na_xMn_{2/3}Fe_{1/3}O_2$ and $Na_xMn_{1/2}Fe_{1/2}O_2$ systems. For both P2 pristine materials, one can assume the following cation distributions, $Na_{0.66}Mn^{3+}_{0.33}Mn^{4+}_{0.34}Fe^{3+}_{0.33}O_2$ and $Na_{0.62}Mn^{3+}_{0.12}Mn^{4+}_{0.38}Fe^{3+}_{0.5}O_2$, which are in agreement with the Mössbauer characterization.

Electrochemical discharge/charge curves, show globally similar voltage profiles with in discharge a voltage plateau at 2.15 V associated to the Mn^{4+} reduction to the trivalent state. In charge, the Mn^{3+} ions are oxidized to the Mn^{4+} for both materials.

In the case of the $Na_xMn_{1/2}Fe_{1/2}O_2$, the iron oxidation starts when the manganese oxidation is completed as evidenced by the GITT curve which shows a strong resistivity increase at the $Na_{0.50}Mn_{1/2}Fe_{1/2}O_2$ composition. When the material contains only Mn^{4+} and Fe^{3+}, the electronic transfer is very difficult. Electron hopping between these two ions requires the intermediate formation of Mn^{3+} and Fe^{4+} that is very unlikely due to the difference in redox potential. For smaller amount of sodium when the $Fe^{3+/4+}$ couple is involved there is a rapid increase of voltage.

On the contrary, for the $Na_{1/3}Mn_{2/3}Fe_{1/3}O_2$ composition, the increase of resistance is very low and the change in voltage is smoother. This suggests that there is an overlapping between the $Mn^{4+/3+}$ and $Fe^{4+/3+}$ redox couple. In a triangular lattice, each M cation is surrounded by six other M cations. When a large cation (Fe^{3+}) is surrounded by a large number of small cation (Mn^{4+}) there

is an increase of the crystal field which makes easier the iron oxidation; the largest the number of Mn ions in the material is, the easiest the oxidation of iron is.

The Mossbauer characterization shows the iron oxidation at high voltage and in particular the presence of the intermediate oxidation state Fe^{3+z} which is due to the rapid electron hopping between neighbouring Fe^{3+} and Fe^{4+} ions. The relative presence of the three types of iron depends on the iron/manganese distribution and of the average oxidation state of iron imposed either by the sodium amount or by the Fe/Mn ratio. The determination of the various population of tetravalent iron agrees in first approximation to the expected results: the iron oxidation occurs after the manganese oxidation.

For both materials, when the Na amount is smaller than 0.30 there is a pseudo voltage plateau, which is associated to a rapid decrease of the interslab distance with an asymmetry of the (002) line to the high 2θ values which suggests the formation of stacking faults. For the lowest sodium amount there is an increase of the M-O bond covalency, which decreases the effective charge of the oxygen ions; it results a decrease of the repulsions between the two oxygen layers surrounding a Na^+ layer. The trigonal prismatic Na^+ environment is no longer stable and a slab gliding occurs to form an octahedral surrounding. In the literature, the formation of O2 and OP4 packing is considered[20,11]. In fact, the XRD patterns exhibit only few lines, which can be indexed in the O2, O6 and OP4 structural types. In fact, if the O2 or O6 type structures were obtained, the interslab distances should be much shorter than that found in the Z- phase (5.1-5.2 Å). The slab gliding, which occurs to form octahedral type interslab spaces, occurs randomly leading to a material with a high amount of stacking faults which is called the "Z" phase in this paper.

At the end of discharge, all cations are in the trivalent state. The Jahn-Teller effect on Mn^{3+} ions locally leads to a distortion of the MnO_6 octahedron. On the opposite, the Fe^{3+} ions are strongly stabilized in undistorted FeO_6 octahedra. The cooperative distortion, which leads to a decrease in symmetry from $P6_3/mmc$ to Cmcm, is directly related to the Mn/Fe ratio and to the number (1-x) of remaining Mn^{4+}, ions in the $Na_x(Mn,Fe)O_2$ phase. In the $Na_xMn_{1/2}Fe_{1/2}O_2$ system the cooperative distortion is observed for x = 0.94, while in the $Na_xMn_{2/3}Fe_{1/3}O_2$ one it appears for the intermediate composition x = 0.74 thanks to the higher Mn/Fe ratio.

To discuss the impact of the Mn/Fe ratio on the structure of fully intercalated materials, we compared results obtained from our previous and current studies and those of the literature (O3-$NaFeO_2$[47] and O'3-$NaMnO_2$[45]). As shown in **Figure 8a**, the $a_{mon.}/b_{mon.}$ and $b_{orth.}/a_{orth.}$ ratios

increase with the Mn^{3+} content: from 1.73 (O3-$NaFeO_2$, no cooperative Jahn-Teller effect [47]) to 1.88 (P'2-$Na_{0.96}Mn_{2/3}Fe_{1/3}O_2$). One can observe a gap between the actual $a_{mon.}/b_{mon.}$ ratio of O'3-$NaMnO_2$ (1.99) and the one obtained by extrapolating from our experimental data (1.96). This difference results from the fact that there is only Mn^{3+} in O'3-$NaMnO_2$. One can conclude that the presence of other ions (such as Fe^{3+}) restricts the cooperative Jahn-Teller effect even if their amount is very small. The increasing distortion is confirmed in **Figure 8b** that reports the evolution of the M-O distances in the MO_6 octahedra for O'3-$Na_{0.96}Mn_{1/3}Fe_{2/3}O_2$[16], P'2-$Na_1Mn_{1/2}Fe_{1/2}O_2$[17], P'2-$Na_{0.96}Mn_{2/3}Fe_{1/3}O_2$ and O'3-$NaMnO_2$[45]. As one can see, the MO_6 distortion increases with the overall Mn^{3+}. It is interesting to note that the long M-O distance increases strongly with the Mn^{3+} content while the short M-O distance remains approximatively equal to the average sum of the ionic radii.

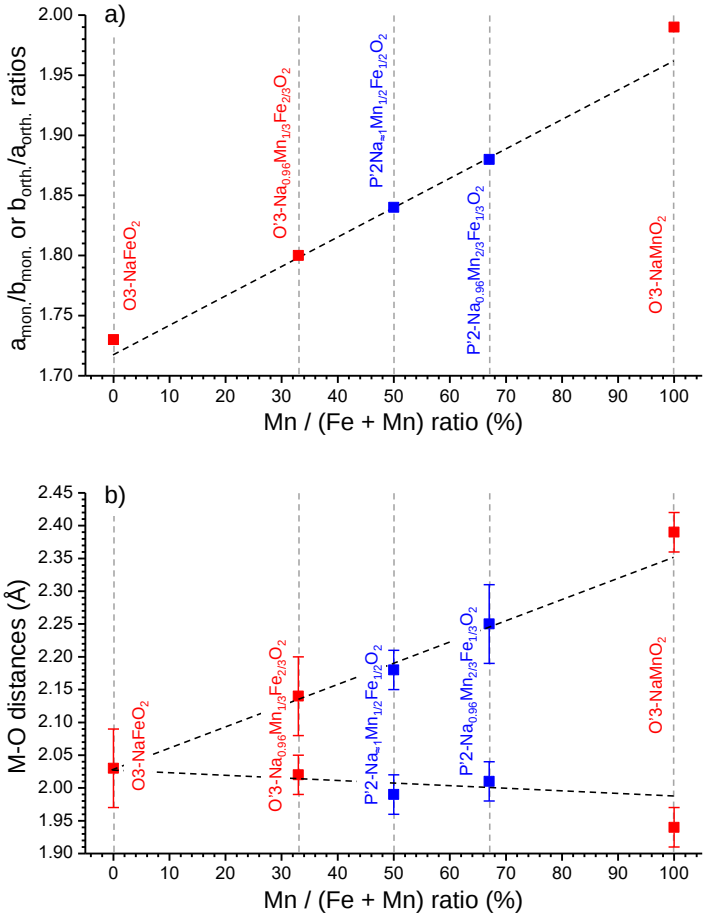

Figure 8: (a) Evolution of the $a_{mon.}/b_{mon.}$ or $b_{orth.}/a_{orth.}$ ratios along with the Mn content in the $Na_xMn_{1-y}Fe_yO_2$ materials. O3-$NaFeO_2$: data from ref 47, O'3-$NaMnO_2$: data from ref 45. (b) Evolution of the M-O distances in the MO_6 octahedra in P'2 and O'3-$Na_{\approx 1}Mn_{1-y}Fe_yO_2$ phases and in O'3-$NaMnO_2$.

This increasing distortion of the MO_6 octahedra is also observed by ^{57}Fe Mossbauer spectroscopy **(Fig. 7 and Table 2)** which shows an increase of the average quadrupole splitting from P'2-$Na_1Mn_{1/2}Fe_{1/2}O_2$ ($\Delta^* = 0.98$ mm.s^{-1}) to P'2-$Na_{0.96}Mn_{2/3}Fe_{1/3}O_2$ ($\Delta^* = 1.31$ mm.s^{-1}), in agreement with the higher disorder of the latter.

The complete phase diagrams of the $Na_xMn_{2/3}Fe_{1/3}O_2$ and $Na_xMn_{1/2}Fe_{1/2}O_2$ systems deduced from *in situ* XRPD are given in **Figure 9**. The comparison of the 2 phase diagrams shows that the amount of sodium reversibly involved in the intercalation process are very similar even if there is shift in the global compositions. In both side of the P2-solid solution domains there are structural modifications with formation of intermediates phases. At high voltage there are slab gliding with change in the interslab distances while no significant modification of the $(Mn,Fe)O_2$ slabs are expected. On the contrary at low voltage, thanks to the Jahn-Teller of Mn^{3+}, there are local distortions of the $(Mn,Fe)O_2$ slabs without change in the interslab distance. In the case of the $(Mn_{2/3}Fe_{1/3})$ system, the appearance of an intermediate distorted phase with a small distortion would lead to a decrease of the structural constraints and then to decreases the fading upon cycling.

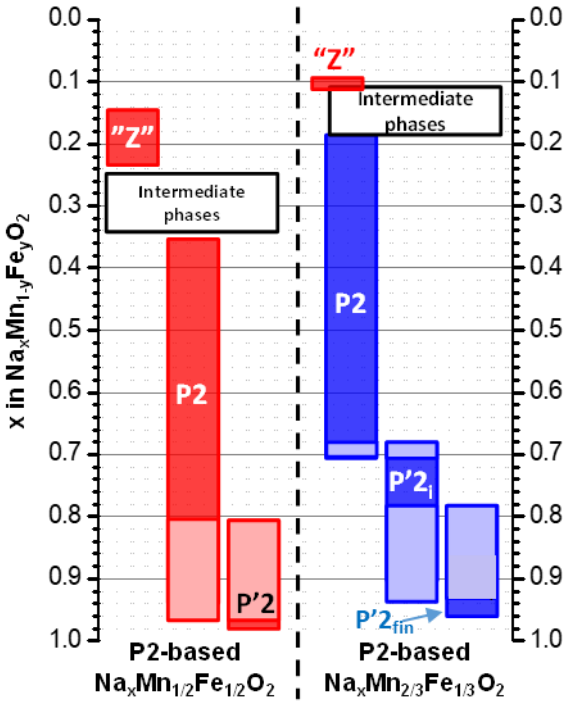

Figure 9: Domains of observation of the P'2, P2 and "Z" phases (P2-type materials) in the $Na_xMn_{2/3}Fe_{1/3}O_2$ and $Na_xMn_{1/2}Fe_{1/2}O_2$ systems.

Conclusion

The electrochemical performances of the two systems are very similar; nevertheless, the Mn/Fe ratio has a significant influence on the redox process. The P2 type structure with hexagonal symmetry is maintained in a Δx = 0.50 domain. As expected the Mn^{3+} oxidation occurs before the Fe^{3+} one. In fact, the GITT curves show that the behavior is more complicated. In the $Na_xMn_{1/2}Fe_{1/2}O_2$ system, this rule is respected while in the case of the $Na_xMn_{2/3}Fe_{1/3}O_2$ system the high crystal field around the Fe^{3+} ions due to the small size of Mn^{4+} and its high concentration leads to Fe^{3+} oxidation before the complete oxidation of Mn^{3+}. The Mossbauer characterization shows the iron oxidation at high voltage with the simultaneous presence of Fe^{3+}, Fe^{4+} and Fe^{3+z}. The easier oxidation of iron, when the amount of manganese increases, leads to a capacity increase.

For the high level of deintercalation, the almost empty trigonal prismatic sites are destabilized and slab gliding occurs to minimize the oxygen-oxygen repulsions trough the formation of empty octahedral interlayered spaces. This slab gliding occurs statistically into the P2 type packing; it leads to the formation of an interstratified structure. These structural transitions lead a rapid decrease on the reversible capacity.

During the cell discharge there is a cooperative Jahn-Teller distortion. This is a well-known phenomenon for the fully intercalated materials. In the case of the $Na_xMn_{2/3}Fe_{1/3}O_2$ phase, for the first time, an intermediate distorted phase was observed. This can result from the competition between Mn^{3+} which want to be distorted and Fe^{3+} which is very stable in undistorted octahedra. This can be related to local fluctuations in composition. In conclusion, due to their interesting properties, the $Na_xMn_{2/3}Fe_{1/3}O_2$ material can be considered as a base to improve its properties to be used in real systems.

Associated content

Supporting in formation

The Supporting information is available free of charge on the ACS Publications website at DOI:

The supporting results provided in Figures S1-S5 give: structural data of the starting phases, their changes upon electrochemical deintercalation ad complementary results about the in situ XRD study.

Author information

Corresponding Author

*E-mail: claude-henri.delmas@icmcb.cnrs.fr

Orcid

Claude Delmas: 0000-0002-8188-0067

Author contribution

The manuscript was written through contributions of all authors. All authors have given approval of the final version of the manuscript.

Notes

The authors declare no competing financial interest.

Acknowledgments

The authors thank Cathy Denage for technical assistance. This work beneficiated from a grant from Agence Nationale de la Recherche (Blanc Inter II, SIMI 8) no. 2011-IS08-01. Region Aquitaine and CNRS are also acknowledged for B.M. scholarship. This research used resources of the Advanced Photon Source, a U.S. Department of Energy (DOE) Office of Science User Facility operated for the DOE Office of Science by Argonne National Laboratory under Contract No. DE-AC02-06CH11357.

References

1. Yang Z.; Zhang J.; Kinter-Meyer M.; Lu X.; Choi D.; Lemmon J.; Liu J;. Electrochemical energy storage for green grid. *Chem. Rev.* **2011**, *111*, 3577-3613.
2. Palomares V.; Serras P.; Villaluengal.; Hueso K.; Carretero-Gonzalez J.; Rojo T. Na-ion batteries, recent advances and present challenges to become low cost energy storage systems. *Energy Environ Sci.* **2012**, *5*, 5884-5901.
3. Ellis B.; Nazar L. Sodium and sodium-ion energy storage batteries. *Curr. Opin. Solid State and Mat. Sci.* **2012**, *16*, 168-169.
4. Nithya C.: Gopukumar S. Sodium ion batteries: a newer electrochemical storage. *Wiley Interdiscip. Rev.: Energy Environ.* **2015**, *4*, 253-278.
5. Yabuuchi N.; Kubota K.; Dahbi M.; Komaba S. Research development on sodium –ion Batteries. *Chem. Rev.* **2014**, *14*, 11363-11682.

6. Kim H.; Kim H.; Ding Z.; Lee M.; Lim K.; Yoon G.; Kang K. Recent progress in Electrode Materials for sodium- ion Batteries. *Adv. Energy Mater.* **2016**, *6*, 1600943-1600981.
7. Hwang J-Y. ; Myung S-T.; Sun Y-K. Sodium-ion batteries; present and future. *Chem. Soc. Rev.* **2017**, *46*, 3529-3614.
8. Kubota K.; Yabuuchi N.; Yoshida H.; Dahbi M.; Komaba S. Layered oxides as positive electrode materials for Na- Batteries. *MRS Bull.* **2014**, *39*, 416-422.
9. Han M-H.; Gonzalo E.; Singh G.; Rojo T. A comprehensive review of sodium layered oxides: powerfull cathodes for Na-ion batteries. *Energy Environ Sci*. **2015**, *8,* 81-102.
10. Clement R.; Bruce P.; Grey C. Review-Manganese-Based P2-type Transition Metal Oxides as Sodium- ion Battery Cathode Materials. *J. Electrochem. Soc*. **2015**, *162(14)*, A2589-A2604.
11. Yabuuchi N.; Kajiyama M.; Iwatate H.; Nishikawa H.; Hitomi S.; Okuyama R.; Isui R.; Yamada Y.; Komaba S. P2-type $Na_x[Fe_{1/2}Mn_{1/2}]O_2$ made from earth-abundant elements for rechargeable Na Batteries. *Nat. Mater.* **2012**, *11*, 512-517.
12. Mortemard de Boisse B.; Carlier D.; Guignard M.; Delmas C. Structural and electrochemical Characterizations of P2 and New O3 $Na_xMn_{1-y}Fe_yO_2$ Phases Prepared by auto-combustion synthesis for Na-ion batteries. *J. Electrochem. Soc.* **2013**, *160(4)*, A569- A574.
13. Thorne J.; Dunlap R.; Obrovac M. Structure and Electrochemistry of $Na_xFe_xMn_{1-x}O_2$ ($0.5<x<1.0$) for Na-Ion Battery Positive Electrodes. *J. Electrochem. Soc.* **2013**, *160(2)*, A361- A367
14. Yoncheva M.; stoyanova R.; Zhecheva E.; Kuzmanova E.; Sendova- Wassileva M.; Nihtianova D., Carlier D.; Guignard M.; Delmas C. Structure and reversible lithium intercalation in a new P'3 phase $Na_{2/3}Mn_{1-y}Fe_yO_2$. *J. Materials Chem.* **2012,** *22*, 23418-23427.
15. Gonzalo E.; Han M.; Lopez del Arno J.; Acebedo B.; Casas-Cabanas M. and Rojo T. Synthesis and characterization of pure P2 and O3 $Na_{2/3}Fe_{1/3}Mn_{1/3}O_2$ as cathode materials for Na Batteries. *J. Mater. Chem.* **2014**, *2*, 18523-18530.
16. Mortemard de Boisse B.; Cheng J; Carlier D.; Guignard M.; Pan G.; Bordere S.; Filiminov D. Drathen C.; Suard E.; Hwang B-J.; Wattiaux A.; Delmas C. O3- $Na_xMn_{1/3}Fe_{2/3}O_2$ as positive electrode material for Na-ion Batteries: structural evolutions and redox mechanism upon Na (de)intercalation. *J. Mater. Chem.* A. **2015**, *3*, 10976-10989.
17. Mortemard de Boisse B.; Carlier D.; Guignard M.; Bourgeois L.; Delmas C. P2- $Na_xMn_{1/2}Fe_{1/2}O_2$ Phase used as positive electrode material for Na Batteries: structural changes induced by the Electrochemical (De)intercalation. *Inorg. Chem.* **2014**, *53*, 11197-11205.
18. Talaie E.; Duffort V.; Smith H;; Fultz B. Nazar L. Structure of the high voltage pause of layered P2-$Na_{2/3-z}[Mn_{1/2}Fe_{1/2}]O_2$ and the positive effect of Ni substitution on its stability. *Energy Environ. Sci.* **2015**, 8,2512-2523.
19. Dose W.: Sharma N.; Pramudita J.; Brand H.; Gonzalo E.; Rojo T. Struture-eletrochemical Evolution of a MnRichP2 $Na_{2/3}Fe_{0.2}Mn_{0.8}O_2$ Na-ion battery material. *Chem. Mater.* **2017**, *29*, 7416-7423
20. Lu Z.; Dahn J. In situ X-ray diffraction Study of P2-$Na_{2/3}[N_{i1/3}Mn_{2/3}]O_2$. *J. Electrochem. Soc*. **2001**, *148(11)*, A1225-A1229.
21. Wang H.; Yang B.; Liao X-Z.; Xu J.;Yang D.; He Y-S.; Ma Z-F.; Electrochemical properties of P2-$Na_{2/3}[Ni_{1/3}Mn_{2/3}]O_2$ cathode material for sodium batteries when cycled in different voltage ranges. *Electrochim. Acta.* **2013**, *113*, 200-204.
22. Yabuuchi N.; Hara R.; Kubota K.; Paulsen J.; Komaba S.; A new electrode material for rechargeable sodium batteries; P2-Type $Na_{2/3}[Mg_{0.28}Mn_{0.72}]O_2$ with anomalous high reversible capacity. *J. Mater.Chem. A.* **2014,** *2*, 16851-16855.
23. Billaud J.; Singh G.; Armstrong R.; Gonzalo E.; Roddatis V.; Armand M.; Rojo T.; Bruce P. $Na_{0.67}Mn_{1-x}Mg_xO_2$ ($0 \leq x \leq 0.2$); a high capacity cathode for sodium-ion batteries. *Energy Environ. SCI*. **2014**, *7*, 1387-1391.

24. Butcholz D.;Vaalma C.; Chagas L.; Passerini S. Mg doping for improved long term cyclability of layered Na-ion cathode materials – the example of P2-type $Na_xMg_{0.11}Mn_{0.89}O_2$. *J. Power Sources*. **2015**, *282*, 581-585.
25. Yabuuchi N.; Yamo M.; Yoshida H.; Kuze S.; Komaba S. Synthesis and Electrode Performances of O3 type $NaFeO_2$-$NaNi_{1/2}Mn_{1/2}$ solid Solution for Rechargeable Sodium Batteries. *J. Electrochem.* Soc. **2013**, *16(5)*, A 3131-A3137.
26. Yuan D.; Hu X.; Qian J.; Pei F.; WU F.; Mao R.; Ai X.; Yanf H.; Cao Y. P2-$Na_{0.67}Mn_{0.65}$ $Fe_{0.2}Ni_{0.15}O_2$ Cathode Material with High-capacity for Sodium-ion Battery. *Electrochim. Acta.* **2014**, *116,* 300-305.
27. High Performance $Na_{0.5}[Ni_{0.23}Fe_{0.13}Mn_{0.63}]O_2$ Cathode for Sodium-ion Batteries. *Adv. Energy Mater*. **2014** , *4*, 1400083-1400090.
28. Carlier D.; Cheng J.; Berthelot R.; Guignard M.; Yoncheva M.; Stoyanova R.; Hwang B.; Delmas C. The P2 type $Na_{2/3}Co_{2/3}Mn_{1/3}O_2$ phase: structure, physical properties and electrochemical behavior as positive electrode in sodium battery. *Dalton Trans.* **2011**, *40*, 9306-9312.
29. Cheng J.; Pan C.; LeeJ.; Guignard M.; Delmas C.; Carlier D.; Hwang B.J. Simultaneous reduction of Co^{3+} and Mn^{4+} in P2-$Na_{2/3}Co_{2/3}Mn_{1/3}O_2$ as evidenced by X-ray Absorption Spectroscopy during Electrochemical Sodium deintercalation. *Chem. Mater.* **2011**, *26*, 1219-1225.
30. Wang X.; Tamaru M.; Okubo M.; Yamada A. Electrode Properties of P2-$Na_{2/3}Mn_yCo_{1-y}O_2$ as cathode materials for Sodium-ion Batteries. *J. Phys. Chem. C*, **2013**, *117*, 15545-15551.
31. Xu, X.; Ji S.; Gao R.; Lui J. Facile synthesis of P2-type $Na_{0.4}Mn_{0.53}Co_{0.46}O_2$ as a high capacity cathode material for sodium-ion batteries. *RSC Adv.* 2015, *5*, 514545-51460.
32. Buchholz D.: Moretti A.; Kloepsch R.: Novak S.; Siosios V.; Winter M.; Passerini S. Toward Na-ion Batteries-Synthesis and Characterization of a novel High Capacity Na-Ion Intercalation Material, *Chem. Mater.* **2012**, *25,* 142-148.
33. Sathiya M.; Hemalatha K.; Tarascon J-M.; Prakash A. Synthesis, Structure and Electrochemical properties of the Layered Sodium insertion Cathode Material: $NaNi_{1/3}Mn_{1/3}Co_{1/3}O_2$. *Chem. Mater.* **2012,** *24*, 1846-1853.
34. Yuan A.; He W.; Pei F.; Wu F.; Wu Y.; Qian J.; Cao Y.; Ai X.; Yang H. Synthesis and electrochemical behaviors of layered $Na_{0.67}[Mn_{0.67}Co_{0.2}Ni_{0.15}]O_2$ microflakes as a stable cathode for sodium- ion Batteries. *J. Mater. Chem. A.* **2013**, *1*, 3895-3899.
35. Doubaji, S.; Valvo M. Saadoune I.; Dahbi M.; Edstrom K. Synthesis and characterization of a new layered material for sodium ion Batteries. *J. Power Sources.* **2014**, *266*, 275-281.
36. Yoshida J.; Guerin E.; Arnault M.; Constantin C.; Mortemard de Boisse B.; Carlier D. Guignard M.; Delmas C. New P2-$Na_{0.70}Mn_{0.60}Ni_{0.30}Co_{0.10}O_2$ Layered Oxide as Electrode Material for Na-ion Batteries. *J. Electrochem. Soc.* **2014**, *161(14)*, A1-A5.
37. Kaliyappan K.; Liu J.; Lushington A.; Li R.; Sun X.; Highly stable $Na_{2/3}(Mn_{0.54}Ni_{0.13}Co_{0.13})O_2$ Cathode Modified by atomic layer deposition for Sodium-ion Batteries. *ChemSusChem*. **2015**, *8*, 2537-2543.
38. Ivanova S.; Zhecheva E.; Kukeva R.; Tyuliev G.; Nihtianova D. Effect of Sodium content on the reversible Lithium intercalation into Sodium-deficient Cobalt-Nickel- Manganese oxides $NaxCo_{1/3}Ni_{1/3}Mn_{1/3}O_2$ ($0.38 < x < 0.75$) with a P3 type of structure. *J. Phys. Chem. C.* **2016**, *120*, 3654-3668.
39. Yabuuchi, N. ; Hara R. ; Kajayama M. ; Kubota K. ; Ishigaki T. ; Hoshikawa A. ; Komaba Shinichi. New O2/P2-type Li-Excess Layered Manganese Oxides as Promising Multi-Functional Electrode Materials for Rechargeable Li/Na Batteries. **2014**, *4*, *Adv. Energy Mater.* 1301453.
40. De la Llave, E. ; Talaie E. ; Levi E. ; Nayak P. ; Dixit M. ; Rao P. ; Hartmnn P. ; Chesneau F. ; Major D.. Greenstein M. ; Aurbach D. ; Nazar L. Improving Energy Density and Structural Stability of Manganese Oxide Cathodes for Na-Ion Batteries by Structural Lithium Substitution. **2016**, *28***,** *Chem. Mater.*, 9064-9076.

41. Delmas C. ; Fouassier C. ; Hagenmuller P. Structural classification and properties of the layered oxides. *Phys. B,* **1980***, 99*, 81-85.
42. Leriche, J. B.; Hamelet, S.; Shu, J.; Morcrette, M.; Masquelier, C.; Ouvrard, G.; Zerrouki, M.; Soudan, P.; Belin, S.; Elkaïm, E.; Baudelet, An Electrochemical Cell for *Operando* Study of Lithium Batteries Using Synchrotron Radiation, *J. Electrochem. Soc.* **2010**, *157 (5)*, A606−A61.
43. Hesse J. ; Rûbartsch A. Model independant evaluation of overlapped Môssbauer Spectra, *J. Phys. E: Sci. Instrum.* **1974**, *7*, 526-532.
44. Berthelot R. ; Carlier D. ; Delmas C. Electrochemical investigation of the P2–Na_xCoO_2 phase diagram, *Nat. Mater.* **2011**, *10(1)*, 74-80.
45. Parant J.P. ; Olazcuaga R. ; Devalette M. ; Fouassier C. ; Hagenmuller P. Sur quelques nouvelles phases de formule Na_xMnO_2. *J. Solid State Chem*. **1971**,*3* 1-11.
46. Prado G. : Fournes L. ; Delmas C. ; On the $Li_xNi_{0.70}Fe_{0.15}Co_{0.15}O_2$ system : An X-ray Diffraction and Mössbauer study. *J. Solid State Chem.* **2001**, *159*, 103-112.
47. Takeda Y. ; Nakahara K. Nishijima M. ; Imanishi N. ; Yamamoto O. Sodium deintercalation from sodium iron oxide. *Mat. Res. Bull*. **1994**, *6*, 659-666.

TOC